Mitigating hydrogen embrittlement via film-like retained austenite in 2 GPa direct-quenched and partitioned martensitic steels

Pallaspuro, Sakari; Fangnon, Eric; Aravindh, S. Assa; Claeys, Lisa; Latypova, Renata; Aho, Niko; Uusikallio, Sampo; Dey, Poulumi; Kömi, Jukka; More Authors

DOI
10.1016/j.msea.2024.146872

Publication date
2024

Document Version
Final published version

Published in
Materials Science and Engineering: A

Citation (APA)
Pallaspuro, S., Fangnon, E., Aravindh, S. A., Claeys, L., Latypova, R., Aho, N., Uusikallio, S., Dey, P., Kömi, J., & More Authors (2024). Mitigating hydrogen embrittlement via film-like retained austenite in 2 GPa direct-quenched and partitioned martensitic steels. *Materials Science and Engineering: A*, *908*, Article 146872. https://doi.org/10.1016/j.msea.2024.146872

Materials Science & Engineering A 908 (2024) 146872

Contents lists available at ScienceDirect

Materials Science & Engineering A

journal homepage: www.elsevier.com/locate/msea

Mitigating hydrogen embrittlement via film-like retained austenite in 2 GPa direct-quenched and partitioned martensitic steels

Sakari Pallaspuro [a,*], Eric Fangnon [b], S. Assa Aravindh [a], Lisa Claeys [c], Renata Latypova [a], Yuriy Yagodzinsky [b], Niko Aho [a], Pekka Kantanen [a], Sampo Uusikallio [a], Tom Depover [c], Marko Huttula [d], Poulumi Dey [e], Jukka Kömi [a]

[a] *Materials and Mechanical Engineering, Centre for Advanced Steels Research, University of Oulu, Finland*
[b] *Materials to Products, Department of Mechanical Engineering, Aalto University, Finland*
[c] *Department of Materials, Textiles and Chemical Engineering, Sustainable Materials Science, Ghent University, Belgium*
[d] *NANOMO, Centre for Advanced Steels Research, University of Oulu, Finland*
[e] *Department of Materials Science and Engineering, Faculty of Mechanical Engineering, Delft University of Technology, the Netherlands*

ARTICLE INFO

Keywords:
Density functional theory
Hydrogen embrittlement
Martensite
Partitioning
Residual austenite
TRIP-Aided steels

ABSTRACT

Advanced (ultra)high-strength steels that utilise bcc-fcc microstructures are appealing solutions for producing a combination of high strength and deformability. However, they are also susceptible to hydrogen embrittlement (HE). As larger less stable retained austenite (RA) can impair mechanical performance, its size and morphology are critical factors for achieving and maintaining the desired properties. Here, we present a combined experimental–density functional theory (DFT) study on HE with medium-carbon direct-quenched and partitioned (DQ&P) martensitic steels with varying vol% and film-thickness of RA, showing significantly improved HE resistance as a function of bcc-enrichment and increasing RA film-thickness. DFT reveals low attraction of hydrogen in bcc-Fe with Al, implying a stronger push towards fcc. Furthermore, the solubility of hydrogen increases dramatically with the carbon-enrichment of fcc-Fe when hydrogen and carbon are second neighbours. The theoretical results explain the observed differences in hydrogen diffusion, trap density, and the consecutively lower HE in Al-DQ&P over Si-DQ&P. Our combined experimental and theoretical study thus highlights the important interplay of bcc and fcc phases and H-uptake within austenite-containing carbon steels.

1. Introduction

Hydrogen (H) diffuses relatively fast but has a low solubility in body-centred cubic (bcc) ferrite. On the contrary, H diffusion is extremely slow in face-centred cubic (fcc) austenite, but at the same time, it can hold several orders of magnitude more H than bcc iron. Microstructures comprising of bcc/near-bcc lath-martensite and a moderate fraction of stabilised retained (or residual when unintentional) austenite (RA) for transformation-induced plasticity (TRIP) have been successfully utilised with low-alloyed 3rd generation advanced (ultra)high-strength steels (AHSS) to improve ductility and toughness [1,2] over essentially martensitic ultrahigh-strength structural steels (UHSS) [3]. An example of these are lean-alloyed direct-quenched and partitioned (DQ&P) steels [4–6], which combine energy-efficient single-stage heating and hot-rolling with interrupted quenching followed by an immediate partitioning step for carbon-enrichment in austenite. DQ&P steels can achieve 2 GPa tensile strength levels combined with good elongation and excellent low-temperature impact toughness with carbon contents between 0.2 and 0.3 wt% [4,6,7].

These steels used as structural components are prone to environmental corrosion and corrosion-induced hydrogen ingress [8,9], which exposes them to hydrogen embrittlement (HE). Because as-quenched and quenched & tempered martensitic steels are extremely susceptible to HE, efforts have been directed towards mitigating HE with increased RA fractions [10–12]. Earlier studies have highlighted the importance of RA coverage for preventing hydrogen from percolating around isolated RA islands [13,14]. Generally, an increased fraction of RA decreases the rate of hydrogen diffusion and increases the number of trapping sites [13–16]. However, many studies show that the presence of RA did not reduce the susceptibility to HE, with examples from CrMo steels [17,18], TRIP steels [11,19,20], supermartensitic stainless steels [21], dual-phase steels [19,22], quenched & partitioned steels (Q&P) [12,

---

[*] Corresponding author.
E-mail address: sakari.pallaspuro@oulu.fi (S. Pallaspuro).

https://doi.org/10.1016/j.msea.2024.146872
Received 12 April 2024; Received in revised form 11 June 2024; Accepted 21 June 2024

22–29], and medium-Mn steels [15,30]. The reason for this susceptibility lies in the mechanical stability and size of RA, and how large a defect/microcrack seed is formed when RA transforms into brittle martensite. The stability of RA can be affected by, e.g., alloying (carbon, manganese, molybdenum) and with reduction of the size of RA [31,32]. Thus, increasing RA vol% increases HE susceptibility due to the growing size of the blocky RA [12,16,22–24,27–29]. With high-RA medium-Mn steels, increasing RA vol% mitigated HE [15], but it can as well increase HE due to different activating failure mechanisms on the bcc-fcc interfaces [30]. An alternative approach would be to maximise the volume fraction and surface area of the film-like retained austenite, whose thickness ranges typically from 10 to 120 nm [16,28,29,33,34]. To achieve this while preventing the formation of large blocky RA, prior austenite grain deforming thermomechanical practices are a viable option [35].

The individual underlying HE mechanisms are challenging to elucidate experimentally due to the complexity of these microstructures, which can bring out various combined effects on different size scales. In contrast to this, atomistic simulations can provide insights into hydrogen interactions with individual microstructural features, thus gaining fundamental understanding for mitigation of HE [36,37]. Hence, the ab-initio simulation techniques based on quantum mechanical approaches are ideal for understanding hydrogen interactions with underlying microstructural features. In this regard, Density Functional Theory (DFT) calculations can provide reliable descriptions of hydrogen solubility under different circumstances [38–40].

So far, the effect of film-like only RA in the absence of larger blocky RA on HE susceptibility has not been investigated. Thus, this study combines in situ hydrogen-charged slow-strain rate tensile testing with thermal desorption spectrometry on martensitic and martensitic-austenitic steels with varying Al/Si alloying to quantify HE as a function of RA fraction and film thickness. Through microstructural characterisation, fractography, and DFT calculations, the behavioural differences and the role of austenite film thickness and elemental additions with regard to making AHSS more resistant to HE are explained, and exceptional resistance against HE at 2 GPa strength levels is shown.

2. Materials & methods

2.1. Materials

The study materials are laboratory-made medium-carbon direct-quenched and partitioned steels alloyed with aluminium (Al-DQ&P) or silicon (Si-DQ&P), and a less RA-containing reference material direct-quenched to room temperature (Si-DQ). Their chemical composition and basic properties are given in Table 1. The lower Si-content of the Al-DQ&P is balanced with an increase in Cr to provide similar level of hardness with the Si-DQ&P. The steels were made by homogenising blocks in a furnace at 1200 °C for 2 h, then laboratory hot-rolling into 12 mm thick plates with a 1 MN Carl Wezel 2-high rolling mill, first with four controlled recrystallisation rolling passes with 0.2 strain above the non-recrystallisation temperature, and then four consecutive 0.2 strain passes below 925 °C with a finish-rolling temperature of ~820 °C. After the final pass, the DQ&P steels were immediately quenched in water with an average cooling rate of 62 °C/s to just above a quench-stop temperature of 175 °C, final few °C cooled in air if needed, at which they were transferred to a large-mass furnace preheated to the same temperature, where the DQ&P plates cooled to room temperature over ~50 h, mimicking slow cooling of coiled strips (same casts and production practice as in Refs. [4,5]). A direct-quenched reference material (Si-DQ) was hot-rolled the same way, but with quenching directly to room temperature after the last rolling pass.

2.2. Experiments and characterisation

Slow strain rate tensile (SSRT) tests were performed in air and under continuous electrochemical hydrogen-charging after pre-charging within the same setup. Rectangular SSRT specimens (Fig. 1 a) were wire-cut by electrical discharge machining to 300 mm long specimens with the gauge part sized 1.0 mm × 5.0 mm × 20 mm (thickness × width × length). All specimens were polished mechanically, finishing with 1200 grit emery paper.

In the case of SSRT tests under hydrogen-charging, the specimens were Teflon taped to expose only the gauge part to hydrogen charging. To introduce varying concentrations of hydrogen (C_H), the specimens were electrochemically pre-charged in 3 % NaCl with adjusted ammonium thiocyanate (NH_4SCN) content between 0.1 and 0.3 %, the applied electrochemical potential between −1.0 and −1.2 V_{SCE}, and the pre-charging time between two and 4 h. Two-hour pre-charging time was experimentally determined to provide near-homogeneous distribution of hydrogen across the thickness of the specimen's gauge part. All the hydrogen-charging parameters are given in Appendix A.

The tensile tests were conducted on a 30 kN MTS benchtop tensile test machine (Fig. 1 b) at an initial strain rate of 10^{-4} s^{-1} until fracture with the engineering strains determined using the cross-head displacement, and true fracture strains were determined from the fracture surface area. To exclude the effect of total flexure of the tensile machine, engineering strain is reported with plastic strain values. After fracture, the gauge parts of the tensile specimens were cut into two parts with pliers. The first was cut for hydrogen concentration measurement, and the second was cleaned and stored in a vacuum chamber for fractography. The hydrogen embrittlement indexes (HEI) were determined based on reduction in area $HEI_{A.}$, Eq. (1), and loss of elongation $HEI_{E.}$, Eq. (2), where AR = area reduction (in air), AR_H = H-charged area reduction, EL = loss of elongation (in air), and EL_H = H-charged loss of elongation:

$$HEI_{A.} = \frac{AR - AR_H}{AR} \times 100\% \tag{1}$$

$$HEI_{E.} = \frac{EL - EL_H}{EL} \times 100\% \tag{2}$$

C_H measurements were performed with thermal desorption spectroscopy (TDS) after the SSRT tests. The specimens were cleaned with distilled water followed by drying with helium gas flow to prevent any formation of moisture on the specimen surfaces before measurements. The measurements of the partial pressure of hydrogen were performed in the ultra-high vacuum (UHV) chamber (1×10^{-9} mbar) coupled with a mass spectrometer. The total time from the end of the tensile test to the furnace in the UHV chamber did not exceed 9 min. All TDS measurements were performed at a heating rate of 10 K/min, and the C_H values were calculated by integrating the area under the desorption rate and temperature curve.

Table 1
Chemical composition (wt%), hardness, and tensile properties as tested with Ø6 mm round bars in Ref. [4] (HV_{10} = Vickers hardness, σ_{ys} = yield strength, σ_{ts} = tensile strength, A = elongation).

	C	Si	Mn	Al	Cr	HV_{10}	[4]: σ_{ys} [MPa]	[4]: σ_{ts} [MPa]	[4]: A [%]
Al-DQ&P	0.30	0.56	2.00	1.10	2.20	537 (±5)	1320	1910	12
Si-DQ&P	0.29	0.99	1.91	0.01	1.00	534 (±5)	1200	1870	12
Si-DQ	0.30	0.99	1.86	0.01	1.01	628 (±5)	1480	2100	10

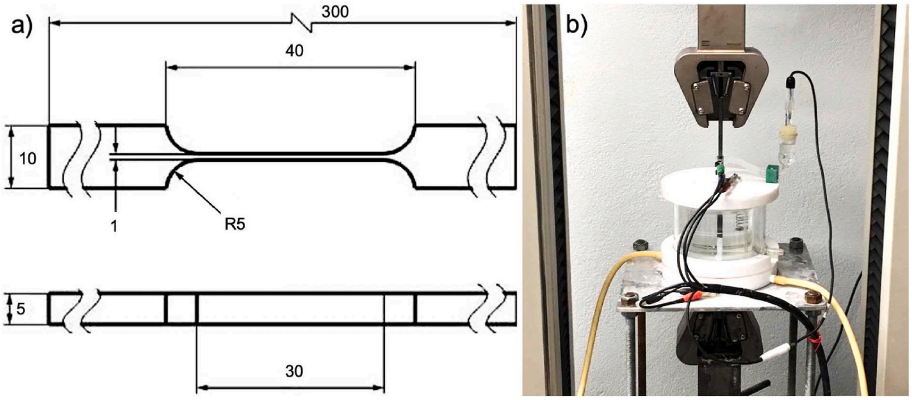

Fig. 1. a) the schematic presentation of the tensile specimens, and b) the test setup.

Electrochemical permeation (EP) was performed using an in-house Devanathan-Stachurski cell setup according to the procedure presented in Ref. [41] to calculate the hydrogen diffusion coefficient (D) using the refined successive transient method [42], reported D values are averages from the four transients, and reversible trapping site density (N_T) was estimated based on the area difference between the experimental and theoretical transient [43]. Both cells were filled with the same 0.1 M NaOH electrolyte with Hg/HgO reference electrode and mixed metal oxide (MMO) mesh counter electrode, potential was varied between −1.1 and −1.2 V for the successive transients, and specimens were ~0.7 mm thick with a 1 μm Pd-coating.

The microstructures were characterised using electron microscopy and X-ray diffraction (XRD). The as-made microstructures and fracture surfaces were characterised with Zeiss Sigma FESEM equipped with an electron backscatter diffraction (EBSD) detector and EDAX-OIM software. EBSD scans were acquired using 15 kV acceleration voltage and 0.05 μm step-size from ion-milled surfaces. Ion-milling was done with JEOL IB-19520CCP cooling cross-section polisher in four refining stages, starting with 8 kV and 270 μA for 4 h, and ending with 3 kV and 38 μA for 8 h. It provided superior EBSD image quality over electrolytic polishing and standard mechanical polishing practice with the last step consisting of colloidal silica gel. Inclusions were mapped with energy-dispersive spectroscopy (EDS) at 15 kV acceleration voltage and 3.5 nA probe current, and classified according to Ref. [44] with minimum inclusion size of 1 μm. Microstructural sub-grain characteristics were investigated with JEOL 2200FS EFTEM operated at 200 kV from thin lamellae extracted from the small sections using focused ion beam, and both bcc lath and fcc film thicknesses were determined from several different thin foils and images for statistical representability. On average, 49 measurements were recorded for each parameter reported in Table 2. The crystallographic properties and retained austenite contents were measured with Rigaku SmartLab 9 kW XRD equipped with a Co anode, and analysed using Rietveld refinement for bct and fcc structures with PDXL2 software. Average carbon contents in retained austenite (C_{RA}) were estimated with the method proposed by Dyson and Holmes [45].

2.3. Theoretical calculations

DFT based simulations were carried out by employing the plane wave-based pseudopotential code, Vienna Ab initio Simulation Package (VASP) [46–48]. Projected augmented wave (PAW) based pseudopotentials were used to describe the interactions between core and valence electrons. The electronic exchange and correlation interactions were described using the generalised gradient approximation (GGA), within the Perdew−Burke−Ernzerhof (PBE) formalism [49]. We employed a cut off energy of 520 eV to expand the plane waves included in the basis set, and respective energy and force tolerances of 1×10^{-6} eV and 1×10^{-3} eV/1×10^{-10} m to achieve the required convergence. The supercell approach was used to model the studied systems taking periodic boundary conditions into account. All the supercells were subjected to full volume relaxation including spin polarisation effects. For both bcc and fcc Fe supercells, a Gamma centred k-point grid of 2 × 2 × 2 was employed. To account for the magnetism, the ferromagnetic state was considered for bcc-Fe and the antiferromagnetic double layer (AFMD) for fcc-Fe.

A 4 × 4 × 4 bcc-Fe supercell was considered, whose base structure contains 128 atoms, and H was introduced at the tetrahedral position (H_{int}). Octahedral site was checked for H_{int} as well, but tetrahedral position was the energetically preferred one for bcc-Fe, as expected. Further, 3 × 3 × 3 fcc-Fe supercell with 108 atoms was considered in which an H atom was introduced at the octahedral position (Fig. 2 a) to compare the preference of formation of H interstitial between bcc and fcc Fe, also with a carbon (C) atom in fcc-Fe as first nearest neighbour (Fig. 2 b) and second nearest neighbour (Fig. 2 c) to H. The formation energies E_{form} are calculated using Eqs. (3) and (4) as given below:

$$E_{form}(bcc / fccFe + x) = E_{total}(bcc / fcc\ Fe + x) - E_{total}(bcc / fcc\ Fe) - \mu(x) \tag{3}$$

$$E_{form}(bcc\ Fe + Al/Si + H) = E_{total}(bcc\ Fe + Al/Si + H) - E_{total}(bcc\ Fe + Al/Si) - \mu(H) \tag{4}$$

In the general form of Eq. (3), the first E_{total} represents the total energy of a bcc/fcc Fe supercell with impurity atoms (i.e., x = H and/or C), the second the total energy of the pristine bcc/fcc Fe supercell, and μ(x) represents the chemical potentials of the impurity atoms i.e. H and/or C. Eq. (4) is for doped bcc/fcc Fe supercells, here containing either Al or Si as substitutional atoms and H as interstitial atom. The chemical potentials of the elements are calculated from the corresponding bulk energies. For the chemical potential of H, the total energy of the

Table 2
Crystallographic properties (XRD) with fcc film and bcc lath thicknesses from TEM investigations (RA = retained austenite, C_{RA} = average carbon content in RA, bcc/fcc = body/face -centred cubic crystallographic structure, c/a = bcc tetragonality).

	RA (fcc) [vol%]	fcc film thickness [nm]	Avg. C_{RA} [wt%]	bcc lath thickness [nm]	bcc c/a
Al-DQ&P	9.4 (±0.2)	67 (±19)	0.63 (±0.02)	148 (±66)	1.0076
Si-DQ&P	9.2 (±0.3)	36 (±14)	0.68 (±0.03)	165 (±49)	1.0078
Si-DQ	2.8 (±0.1)	13 (±4)	0.38 (±0.02)	176 (±73)	1.0084

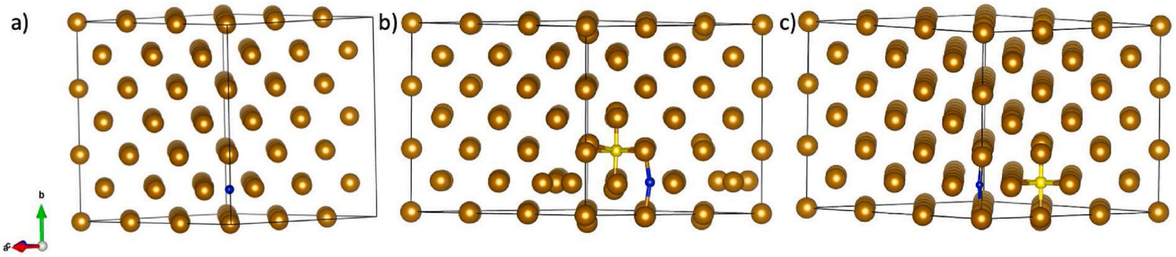

Fig. 2. 3 × 3 × 3 supercells for fcc-Fe (golden) with a) H_{int} (blue) at the octahedral position, b) H_{int} as the first nearest neighbour of a C_{int} (yellow), and c) H_{int} and C_{int} as second nearest neighbours. (For interpretation of the references to colour in this figure legend, the reader is referred to the Web version of this article.)

hydrogen molecule is calculated, and the H atom energy is deduced from that. The chemical potential of C is calculated from the total energy of bulk graphite.

3. Results

3.1. Microstructural characterisation

Si-DQ steel has an auto-tempered lath-martensitic microstructure with a small fraction of very fine inter-lath residual austenite (RA, Fig. 3 a-b), which follows the conventional Kurdjumov-Sachs relationship (111)γ//(011)α'. The microstructures of the DQ&P steels consist of a mixture of low-temperature tempered near-bcc lath-martensite, which has carbon-precipitates due to partial low-temperature tempering during partitioning, and a pronounced fraction of film-like intentionally-produced RA (Table 2, Fig. 3 c-e). Fig. 3 c) show the lath-like microstructures with RA locations highlighted in green. The DQ&P steels contain also similar nano-twinned bcc regions, absent in DQ, but these were omitted here from further analysis. Direct-quenched Si-DQ has a residual austenite (RA) fraction of 2.8 vol%, which increases to 9.2–9.4 vol% with interrupted quenching and partitioning at 175 °C, and without significant difference between the Al/Si alloying (Table 2). In

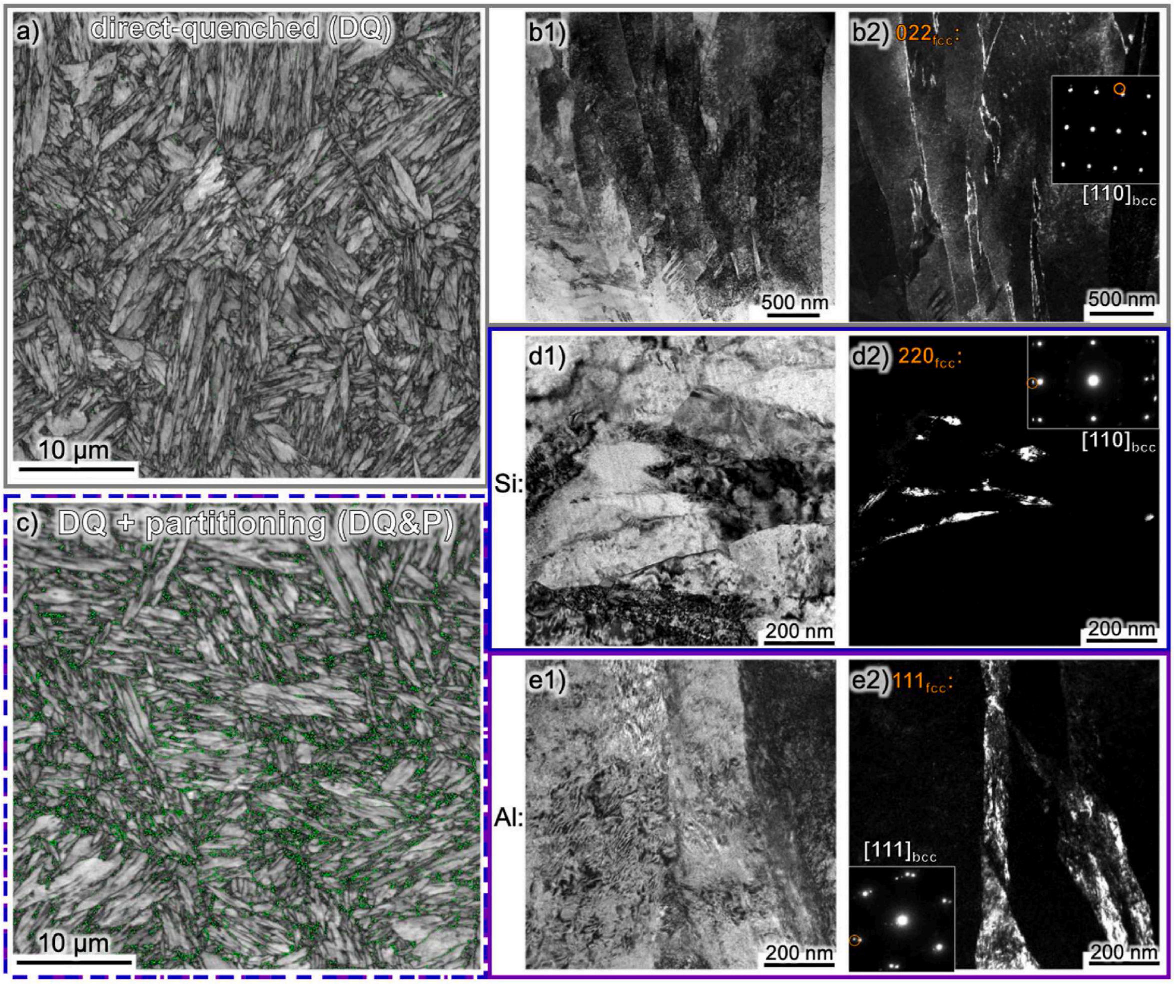

Fig. 3. Microstructure of a) essentially lath-martensitic Si-DQ in EBSD image quality map, b1) bright field TEM image of the lath structure, b2) dark field image of inter-lath residual austenite exited with a 022 fcc spot. Martensitic-austenitic microstructures in c) in image quality map of Al-DQ&P with retained austenite locations shown in green, Si-DQ&P laths and RA films in d1)-d2), and Al-DQ&P with thicker RA films in e1)-e2). (For interpretation of the references to colour in this figure legend, the reader is referred to the Web version of this article.)

Table 2, the thicknesses of fcc films and bcc laths are obtained from TEM investigations, and the rest from XRD data analysis. Similarly, fcc film thickness increases threefold with partitioning from Si-DQ to Si-DQ&P, and this associates to partial decrease in bcc lath thickness. Interestingly, a further almost twofold increase in fcc film thickness occurs with switching to Al-based alloying, changes in bcc lath thickness (Al vs Si) being in line with this change, and slightly lower average carbon content C_{RA} compensating this volumetric expansion. None of the microstructures contain large blocky retained austenite, as the largest individual low-CI indications of retained austenite islands in DQ&P steels are below the effective grain size of ~0.7 μm (0.2 μm threshold for EBSD data).

3.2. *In situ hydrogen-charged tensile tests and thermal desorption spectrometry*

The slow strain rate tensile test results with the TDS-determined hydrogen concentrations C_H (Fig. 5) are summarised in Table 3 and Fig. 4, and the used hydrogen-charging parameters are presented in Appendix A. The steels have a residual hydrogen concentration of ~0.2 wppm, which is marginally higher for Al-DQ&P (0.25 wppm). The steels tested in air reach 1.9–2.1 GPa tensile strength σ_{ts} level, 2.6–2.9 GPa true fracture stress σ_f, and true fracture strain $\boldsymbol{\varepsilon}_f$ of ~0.50. The direct-quenched and partitioned steels have ~200 MPa lower strength values than Si-DQ, generally being in line with the results with 6 mm thick round tensile bars in Ref. [4]. Both DQ&P have similar tensile behaviour as tested in air

All three steels show linear degradation of properties within the given dataset as a function of total hydrogen concentration C_H (Fig. 4 d-f), which consist of both pre-charged hydrogen and uptake during the in situ SSRT tests. However, their behaviour and performance differ dramatically. The low-RA Si-DQ performs the worst, while an increase in RA vol% via partitioning improves the tolerance to hydrogen, however, only slightly within the same alloy (Fig. 4 d-f). Based on the trends, true fracture stress σ_f of Si-DQ drops to 1.5 GPa already with C_H ~1.6 wppm, while at same σ_{ts} level Si-DQ&P tolerates ~2.5 wppm, and Al-DQ&P over twice that with ~6.1 wppm (Fig. 4 d). At maximal measured C_H of ~5.7 wppm, Al-DQ&P reaches still a true fracture strain $\boldsymbol{\varepsilon}_f$ of 0.15. The same trend continues with area-based hydrogen embrittlement index $HEI_{A.}$ – it takes 2.7 x C_H before Al-DQ&P is embrittled to the same degree as DQ&P, and 4.5 x C_H when compared to the low RA-containing direct-quenched Si-DQ (Fig. 4 f).

The TDS results are summarised in Fig. 5. The unstrained specimens accumulate approximately 1 wppm of H during pre-charging, slightly more with higher RA content (Fig. 5 a). The decreasing initial curves below 100 °C come from the most readily effusing interstitial/lattice hydrogen, and the broad main peak (1) at ~190 °C, 183 ± 6 °C for Al-DQ&P and 208 ± 8 °C for Si-DQ&P, from weakly hydrogen trapped hydrogen at dislocations, lath interfaces and grain boundaries, and the pre-existed retained austenite transformed into strain-induced martensite during SSRT testing [50].

A minor high-temperature area (2) around ~410 °C is present in all the materials (Fig. 5). This area (T > 300 °C) of pre-charged specimens (Fig. 5 a) sums to ~0.07 wppm C_H (Fig. 5 a), and after each SSRT test it varies in the range of 0.1–0.2 wppm irrespective of the material (Fig. 5 b-d), so the hydrogen build-up is detected mainly in the first main peak (1). The high-temperature area splits into possible smaller peaks at ~350 °C, ~410 °C, and ~490 °C. These relate to hydrogen in RA (E_a 48–55 kJ/mol [50–52]), likely at RA film interfaces [40–42], and the splitting is likely due to partial transformation of RA [34]. As this peak is present also after the SSRT tests, which consume RA below the lab XRD quantification limit (<1.0 vol%) [4], sampling of the cut pieces for TDS may still contain some untransformed RA further away from the necked failure zone. Complementing explanations of lower vol% present can be inclusions and carbides; bcc-Fe/Fe_3C interface (E_a of 68 kJ/mol [10, 53]), aluminium nitrides (AlN interface E_a ~65 kJ/mol [54]) present in the Al-DQ&P, and manganese sulphides (E_a 72 kJ/mol [55]) present in all three materials. However, verification and quantification of these will require further measurements outside the scope of this study.

The permeation results show that hydrogen diffusion is significantly slower in Al-DQ&P than in the Si-variants (Fig. 6 a). Higher RA film thickness and alloying differences contribute to this ~46 % decrease in D (Al-DQ&P vs. Si-DQ&P), and the 6.6 vol% increase in RA attributes to the ~26 % decrease in D (Si-DQ&P vs. Si-DQ). All the study materials are on the lower bound as compared to diffusion coefficients presented in the literature.

The trap densities (N_T) follow an inverse trend compared to diffusion coefficients: Al-DQ&P has the highest N_T, followed by Si-DQ&P and Si-DQ. This difference between DQ&P steels is largely accounted to the abovementioned differences in RA and precipitates/inclusions, and partly elemental differences in bcc and fcc (see 3.3 DFT study). The higher RA vol% explains the ~43 % increase in N_T between DQ & DQ&P states.

The uncharged specimens tested in air endure pronounced uniform necking before failing in essentially ductile manner, shown in magnified sections in Fig. 7 a, c, e. The fracture surfaces consist of sheared edges and multi-void coalesced (MVC) dimples in the final central ruptured area, and also pronounced secondary cracking due to extreme local hardening of the microstructures ($\sigma_f > 2.6$ GPa). Both Al-DQ&P (Fig. 7 a) and Si-DQ&P (Fig. 7 c) share similar dimple size distributions, here shown with two extremes. As-quenched Si-DQ has more brittle features and flatter dimples than the DQ&P variants.

Hydrogen-charging shifts the predominant failure mechanism to

Table 3

Total hydrogen concentrations (C_H) and slow strain rate tensile test results (σ_{ts} = engineering tensile strength, σ_f = true fracture stress, $\boldsymbol{\varepsilon}_f$ = true fracture strain, AR = reduction of area, $HEI_{A.}$ = hydrogen embrittlement index (HEI) based on the reduction of area, Eq. (1), $HEI_{E.}$ = HEI based on loss of elongation, Eq. (2)).

	C_H [wppm]	σ_{ts} [MPa]	σ_f [MPa]	$\boldsymbol{\varepsilon}_f$	AR [%]	$HEI_{A.}$ [%]	$HEI_{E.}$ [%]
Al-DQ&P, in air	0.25	1880	2602	0.53	41.2	–	–
Al-DQ&P, H 4.2	4.23	1598	1911	0.25	21.8	47.1	53.7
Al-DQ&P, H 5.1	5.07	1462	1656	0.16	14.6	64.6	70.4
Al-DQ&P, H 5.7	5.67	1477	1585	0.15	13.9	66.4	71.9
Si-DQ&P, in air	0.21	1924	2620	0.50	39.4	–	–
Si-DQ&P, H 1.6	1.64	1662	1929	0.21	19.1	51.5	57.7
Si-DQ&P, H 1.7	1.72	1617	1706	0.13	12.2	69.0	74.0
Si-DQ&P, H 2.0	1.97	1496	1669	0.13	12.6	68.1	73.2
Si-DQ&P, H 3.0	2.98	1468	1406	0.05	5.2	86.8	89.3
Si-DQ, in air	0.18	2080	2859	0.52	40.8	–	–
Si-DQ, H 1.3	1.34	1607	1762	0.13	11.9	70.7	75.7
Si-DQ, H 1.4	1.42	1535	1668	0.10	9.3	77.1	81.3

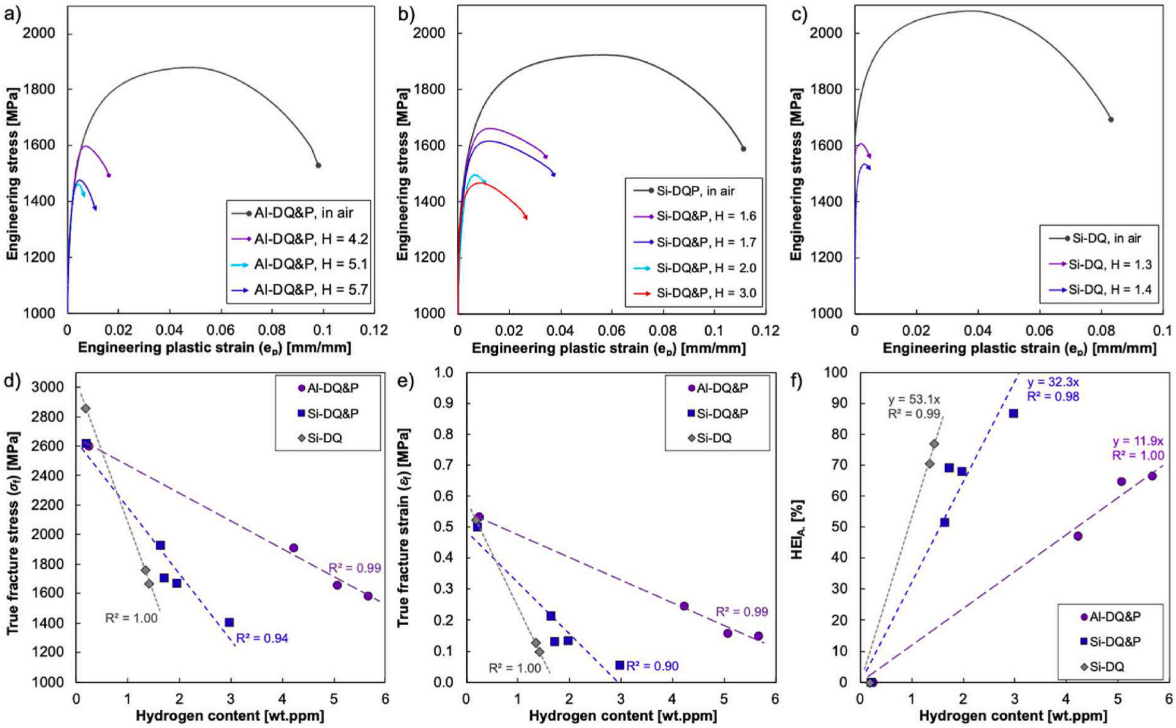

Fig. 4. The slow strain rate tensile test results: flow curves with plastic strain as tested in air and with constant hydrogen-charging a) Al-DQ&P, b) Si-DQ&P, and c) Si-DQ. On the bottom row, the results summarised as a function of hydrogen content: d) true fracture stress, e) true fracture strain, and f) hydrogen embrittlement index (HEI_{A_r}).

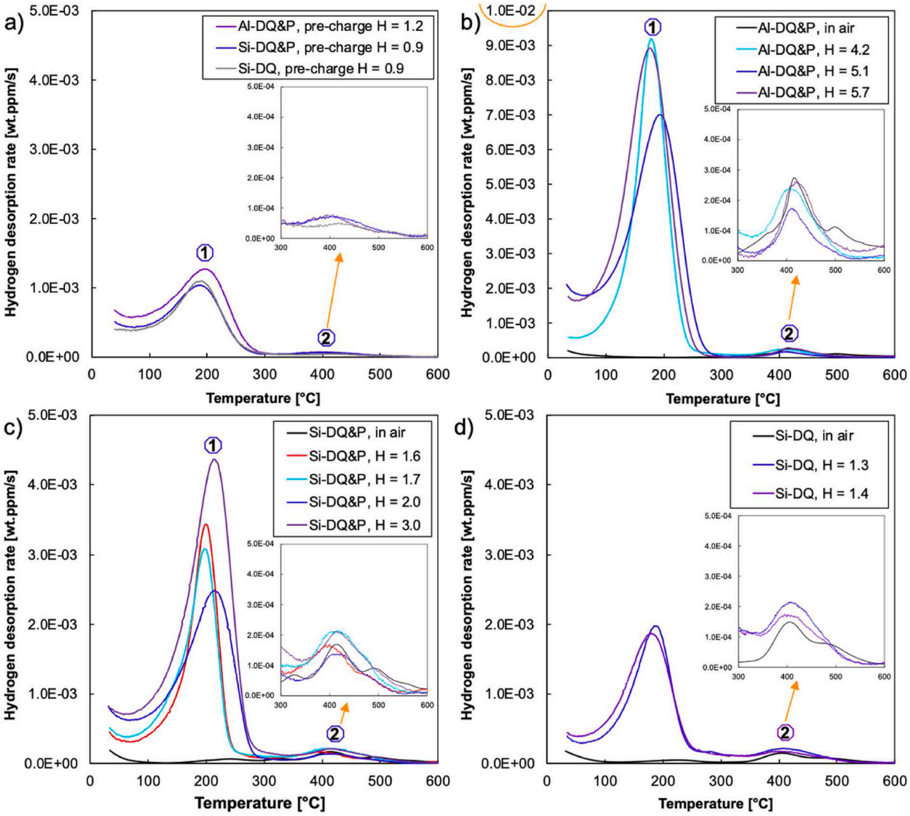

Fig. 5. TDS analysis of a) unstrained specimens with 3 % NaCl +0.1 % NH_4SCN for 3 h, and results after the SSRT tests for b) Al-DQ&P, c) Si-DQ&P, and d) Si-DQ. Note the higher y-axis with Al-DQ&P in b). (1) main peak at ~190 °C, (2) high-temperature peak area around ~410 °C.

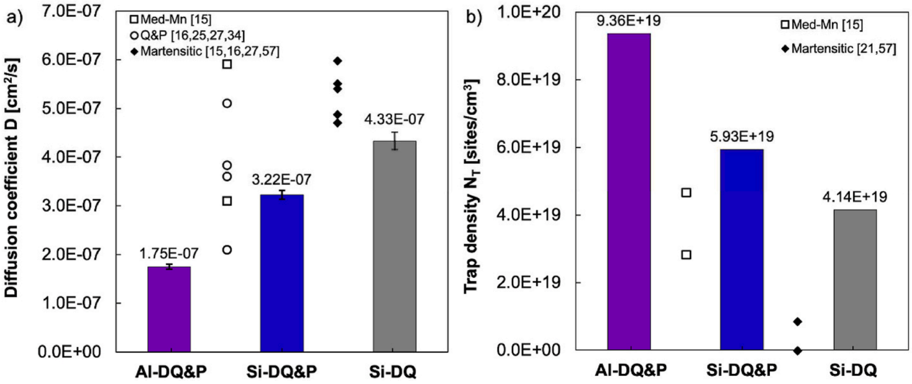

Fig. 6. Hydrogen permeation results with comparison to literature: a) Diffusion coefficients, and b) number of reversible traps. External data: Med-Mn [15], *Q&P* [16,25,27,34]*, and Martensitic* [15,16,27,56] steels.

quasi-cleavage (QC), propagating from the long edges towards the centre (Fig. 7 b1, d1, f1). The remaining ligament failing with shallow-dimpled shearing. The fraction of QC increases with both increasing final hydrogen concentration C_H and embrittlement index HEI, which explains less QC in Al-DQ&P (Fig. 7 b1) over the Si-DQ&P specimens (Fig. 7 d1). Increased C_H produces also atypical rounded intergranular-like fracture (Fig. 7 b3, d3, f3), present in both DQ&P and DQ steels. Compared to specimens tested in air, all the H-charged steels have more blunted microcracks on the fracture surfaces, in addition to similar macroscale secondary cracks on the hardened sheared area (example in Fig. 7 d1).

3.3. DFT study

Table 4 summarises the results of the DFT calculations performed within this study in order to understand the experimentally observed difference in the behaviour of DQ and DQ&P steels when exposed to H, as well as to understand why Al-DQ&P show better HE resistance compared to Si-DQ&P. The obtained formation energy (Eq. (3)) for introducing a H_{int} in pure fcc-Fe is 0.18 eV smaller than in bcc-Fe, which is in good agreement with the difference in the solubility of H in these phases. In both phases, the addition of H is still an endothermic reaction, i.e., requiring an external driving force for dissolving H in bcc or fcc Fe. Our results of H solubilities at octahedral site in fcc-Fe and at tetrahedral site in bcc-Fe are in good agreement with existing DFT work [57,58]. The obtained results of site preference of H in bcc and fcc Fe also agree well with available experiments [59].

To understand the beneficial effect of C partitioning to RA on the lowered susceptibility to HE, we considered fcc-Fe supercells with C and H at different octahedral interstitial positions with respect to each other (Fig. 2). The C interstitial (C_{int}) was modelled together with H interstitial (H_{int}) as first (1nn) and second nearest neighbours (2nn) to understand the preferred distances of co-segregation of these elements in fcc Fe. Based on this study, H_{int} is energetically more favourable than C_{int} in fcc-Fe (Table 4), as is evident from the lower formation energy for the former than the latter. More importantly, the DFT results show that when the C_{int} and H_{int} are present at first nearest neighbour positions, i.e., at 2.7 Å distance (Fig. 2 b), the formation energy increases when compared against C_{int} and H_{int} in fcc-Fe separately. However, when C_{int} and H_{int} are placed at second nearest neighbour positions (Fig. 2 c) in fcc Fe, formation energy drops dramatically to about −3.3 eV, indicating that these defects prefer energetically to stay at 4.1 Å distance with respect to each other. We also investigated the scenario where H_{int} is introduced as second neighbour to C_{int} already present in fcc Fe. The resulted formation energy of −3.74 eV shows that H solubility is even higher in already carbon-enriched fcc-Fe. Our DFT results imply that the C_{int} present in fcc-Fe can dramatically increase the solubility of H in fcc-Fe when the C_{int} and H_{int} are present as second neighbours. This in turn indicates that the amount of diffusible H is lower in the presence of carbon-rich RA, i.e., lower in DQ&Ps than DQ (Table 2), as also shown with permeation experiments (Fig. 6 a).

Next, we computed the solubility of H in Al and Si containing bcc-Fe to explain experimental differences between Al-DQ&P and Si-DQ&P. This reveals that H solubility increases in both cases in Al/Si doped bcc-Fe when compared to pure bcc-Fe, but even more in the presence of Si with a −0.8 eV margin (Table 4). This means that Al-alloyed bcc is less attractive for H as compared to Si-alloyed bcc Fe. A similar trend persists also with slightly tetragonal bct structures (Table 3) for H dissolved in Al and Si containing bct-Fe phase (data not shown for brevity), i.e., H prefers the Si-doped ferritic/martensitic structure over the Al-doped one.

4. Discussion

4.1. Microstructural and mechanical properties

The essential difference direct-quenching produces in conjunction with retained austenite (RA) stabilising partitioning process is that deformation of the prior austenite grains before the directly following cooling step can eliminate large blocky/globular RA grains, resulting in RA that is confined to a film-like morphology, as shown in this study (Fig. 3). However, this can be achieved only with optimal chemical composition and thermomechanical rolling process, as already 0.4 wt% C can start to produce blocky RA during similar thermomechanical processing [6]. Here, the RA contents for DQ&P steels are ~9 vol% (Table 2). It appears that the ~10 vol% RA is close to the maximal volume fraction before blocky RA starts to be present in significant fractions, e.g., in quenched & partitioned steels [12,16,22–29], medium-manganese steels [15,30], and TRIP steels [11,19,20]. This ~10 vol% is also at the approximate percolation threshold determined with high-carbon bainitic steels [14]. In addition to the current study, only Xu et al. [29] have reported steels with only film-like RA morphology below 6 vol% and 50–60 nm thickness, but already 9.5 vol% RA introduced additional blocky RA with non-deformed recrystallised austenite grains.

Film-like RA between hard matrix is beneficial for deformability as it is more stable than larger blocky RA [60], and can prevent H percolation around fcc more effectively [14], and once transformed to martensite, acts as a shorter brittle feature for microcrack initiation and propagation. In this study, the RA film thicknesses ranges between 13 and 67 nm (Table 2), being in the middle of typical range [16,28,29,34], indicating that thicker films can be achieved (Fig. 3 e2), and that it is the absence of blocky RA that highlights the here achieved mechanical properties. Furthermore, evenly distributed film-like RA maximises the RA surface

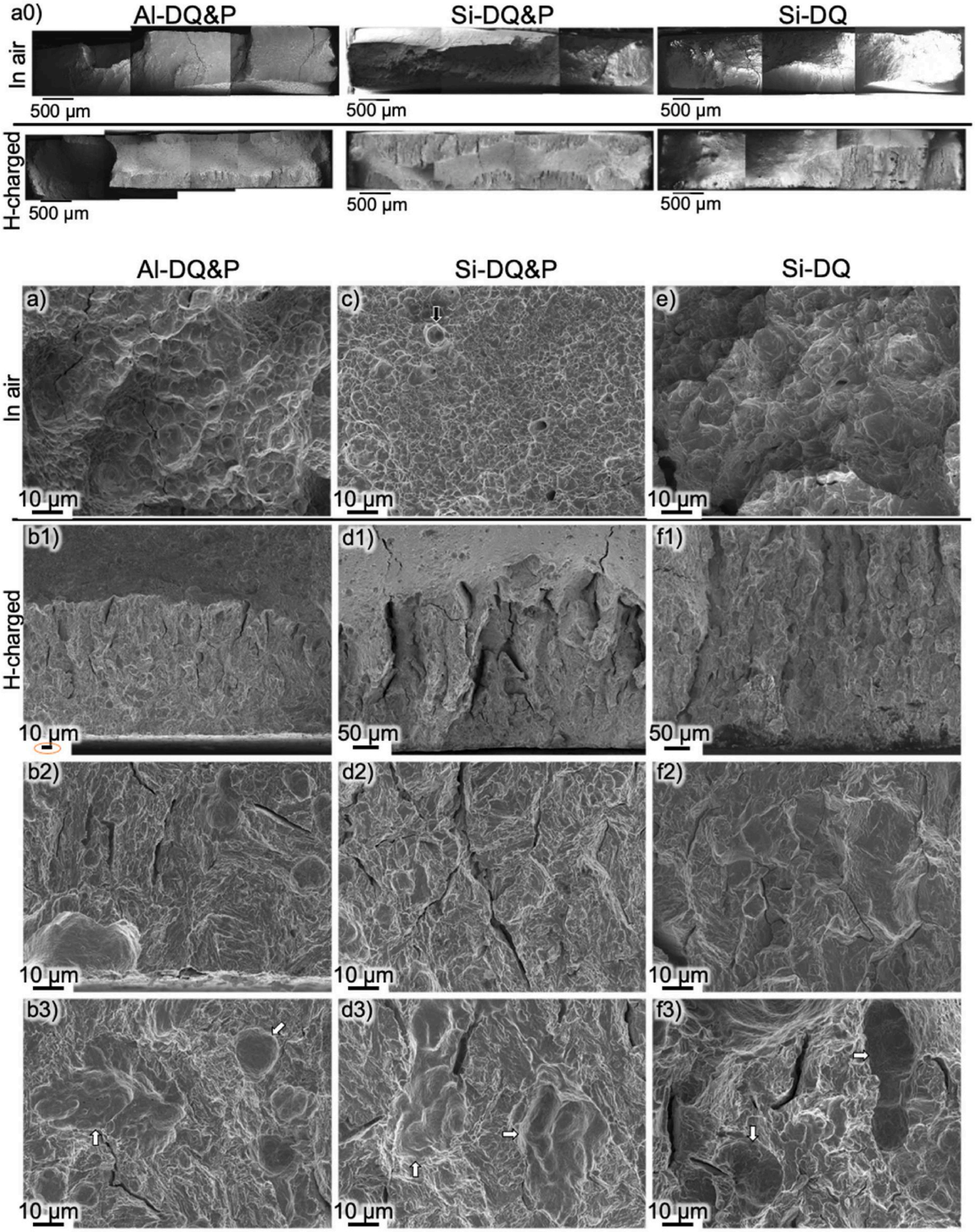

Fig. 7. a0) The tensile specimens after testing in air/hydrogen-charged. Representative fracture surfaces of uncharged tensile specimen (a, c, e) with multi-void coalesced ductile fracture and secondary cracking, and hydrogen-charged specimen (b, d, f) with quasi-cleavage, intergranular-like fracture, and secondary microcracks: b1-b3) Al-DQ&P H 5.7, d1) Si-DQ&P H 3.0, d2-d3) DQ&P H 2.0, f1-f3) Si-DQ H 1.3. White arrows in b3), d3), and f3) point to abnormal intergranular-like features. A typical AlO-based inclusion (black arrow) in c) Si-DQ&P.

Table 4
Density functional theory calculations of H interaction with bcc, and fcc Fe phases (1nn = first nearest neighbour, 2nn = second nearest neighbour).

	Supercell	Formation energy [eV]	
		1nn	2nn
H in bcc	bcc-Fe (4 × 4 × 4, 128 atoms)	–	
	bcc-Fe + H_{int}	0.22	
	bcc-Fe + Al + H_{int}	−0.65	
	bcc-Fe + Si + H_{int}	−1.44	
H and/or C in fcc:	fcc-Fe (3 × 3 × 3, 108 atoms)	–	
	fcc-Fe + H_{int}	0.04	
	fcc-Fe + C_{int}	0.48	
	fcc-Fe + C_{int} + H_{int}	2.12	−3.26
	(fcc-Fe + C_{int}) + H_{int}		−3.74

area, also absorbing H more readily under stresses [34]. As the Si-DQ&P and Al-DQ&P have similar RA vol% but Al-DQ&P has clearly thicker RA films (Table 2), it is possible based on stereology that the true scatter in Al-DQ&P RA film thickness is still larger than what was observed here with TEM from multiple thin foils. On the contrary, assuming that film-thicknesses are true, it could be that the surface-sensitive XRD measurements yield inaccurate RA vol% estimates due to varying crystallographic unit proportions. For example, high-energy XRD measurements or quantitative atom-probe tomography could provide additional insight into this question. Whether RA surface area would be more crucial than film-thickness, the surface area of RA in Al-DQ&P does not increase compared to Si-DQ&P, based on a simple assumption of ellipsoid core-shell structure of bcc-laths and fcc-films (Table 2). Unfortunately, quantification of surface area differences with EBSD is impossible due to insufficient resolution.

Comparison of TDS-spectra and H desorption peaks related directly to RA between the unstrained samples (Fig. 5 a) and after the SSRT tests (Fig. 5 b-d) shows that unstrained film-like RA isn't effective in binding H in given conditions, as also shown by Vercruysse et al. [28]. Same has been observed recently also for blocky RA [34]. This indicates that RA can be beneficial in real life stressed applications exposed to H, as long as local peak stresses stay below a level that causes strain-induced transformation of RA. Furthermore, with the same charging conditions (0.1 % NH_4SCN, 1.0 V_{SCE}, 2 h pre-charging), Si-DQ&P absorbed only ~0.24 wppm more hydrogen than Si-DQ before failure, indicating that its significantly higher RA content is not effective in absorbing H in the given conditions. On the contrary, less attraction of Al-enriched bcc-Fe must drive H more effectively to strained RA, explaining the significantly higher main TDS peaks for Al-DQ&P (Fig. 5 b), which includes RA transformed into martensite. The average main peak, peak (1) in Fig. 5, of Al-DQ&P is characterised by a significantly lower temperature (183 ± 6 °C compared to 208 ± 8 °C of Si-DQ&P), which should be due to the Al/Si bcc alloying differences. The previously reported higher binging energy of a Si atom trapping energy $E_b > 20$ kJ/mol [61] over Al atom $E_b = 6$ kJ/mol in fcc [62], permeation results (Fig. 6) and the DFT results (Table 4) support this finding further. Thus, enrichment of bcc-Fe can have significant effects on the resulting hydrogen diffusion and detrapping. Further future investigations must be executed to distinguish the other high-temperature peak contributions between RA peak splitting [25], inclusions and precipitates.

Interestingly, as a result of the maximised film-like RA vol% and hard martensitic matrix, the microstructures produced here gain both lower hydrogen diffusion coefficients D and higher trap densities N_T than comparable quenched & partitioned steels [16,25,27,34] and martensitic steels [15,16,27,56] (Fig. 6). Prior austenite grains deformed below given non-recrystallisation temperatures (Section 3.1) cause also what appears to be atypical globular intergranular fracture on predominantly individual prior austenite grains (Fig. 7 b3, d3, f3), clearly differing from common hydrogen-induced intergranular fracture [63,64] with slanted facets of recrystallised and freely grown grains. If the underlying mechanisms remain the same, the globular intergranular fracture should consume more energy in the failure process due to higher surface area. All the here studied steels showed this feature, qualitatively more in RA-rich DQ&Ps, indicating that the RA films can play a role in the given failure process – something that demands further investigations. Generally, the DQ and DQ&P steels show that increase in HE comes with increased fraction of quasi-cleavage and decrease in sheared area. RA can be seen as beneficial also considering the frequent blunted micro-cracks present in all the materials (Fig. 7 b3, d3, f3).

4.2. Insights from density functional theory calculations

The DFT calculations revealed that (a) C_{int} and H_{int} prefer energetically to be as second neighbours in fcc-Fe, and (b) H solubility increases significantly in the presence of Al and Si in bcc Fe as compared to pure bcc Fe (Table 4). The same has been previously reported for Al in fcc [37]. The strong attractive interaction between C_{int} and H_{int} as second neighbours in fcc Fe (−3.74 eV), along with higher C_{RA}, result in lesser amount of diffusible H and higher trap density in the DQ&P than DQ steel (Fig. 5).

To explain the experimental observation of Al-DQ&P being better HE resistant than Si-DQ&P, we compared DFT-obtained H solubilities in the presence of either Al or Si in bcc-Fe as a first neighbour of H with that of H solubility in pure bcc Fe. Results reveal that H solubility increases significantly in the presence of both Al (−0.65 eV) and Si (−1.44 eV) in bcc Fe as compared to pure bcc Fe (+0.22 eV). This in turn implies that the uptake of H can be enormously increased by alloying with Al and/or Si. Moreover, the solubility of H increases significantly more in the presence of Si as its first neighbour than Al in bcc Fe, which implies a lesser amount of H in fcc phase for Si-DQ&P. This indicates a higher gradient of H concentration in the Si-containing case than in the case of Al addition, which can in turn explain the experimental observation of Al-DQ&P being better HE resistant than Si-DQ&P. Generally, combining both experimental and DFT results corroborate the fact that more H can get dissolved in DQ&P as compared to DQ. The lesser amount of easily diffusible H in DQ&Ps can explain its better resistance to HE over DQ.

4.3. Hydrogen embrittlement in laminar martensitic-austenitic structures

Fig. 8 Shows the performance of various types of high-strength steels and (advanced) ultrahigh-strength steels with an inverse banana-diagram trend. The data consists of SSRT tests executed with strain rates from 10^{-2} to 10^{-5}, and LIST tests by Liu et al. [22,25], with an average total hydrogen concentration of 3.4 ± 3.6 wt ppm after the tests. Our results presented here belong to the middle of these ranges. Compared to the literature, the here-studied alloys have outstanding performance: already 2080 MPa σ_{TS} DQ tested here is reasonably resistant to HE, and below 70 % HEI_A (Eq. (1)). level, and compared to the literature, up to 800 MPa higher tensile strength can be achieved at similar $HEI_{A.}$ with Al-alloyed martensitic-austenitic steel (Al-DQ&P) with thick film-like inter-lath retained austenite (Fig. 8 a). Even disregarding strength differences, $HEI_{A.}$ is suppressed by one-third compared to nearest results by Yang et al. [24] with similar alloying and pre-charged $C_H \approx 1$ wppm. These trends and differences persist even with elongation-based HEI_E (Eq. (2)). as the measure (Fig. 8 b). These properties can be achieved with prior-austenite grain structure deforming production-practises, like the here-utilised direct-quenching & partitioning process. Interestingly, the closest-performing rivals from the literature are quenched and tempered steels by Yang et al. [24] and quenched & partitioned steels by Yang et al. [24] and Wang et al. [26], both possessing a notable fraction of blocky RA.

The dataset presented in Fig. 8 is unanimous in that blocky RA makes the low-alloyed and medium-alloyed steels more susceptible to hydrogen embrittlement. With low RA content (<2 vol%), HEI varies between 5 % and 100 %, the lowest values presented in Fig. 8 with undisclosed pre-charged/final C_H. With notable RA contents, lowest HEI values are achieved with ~10 %, and data from 12 % upwards show that

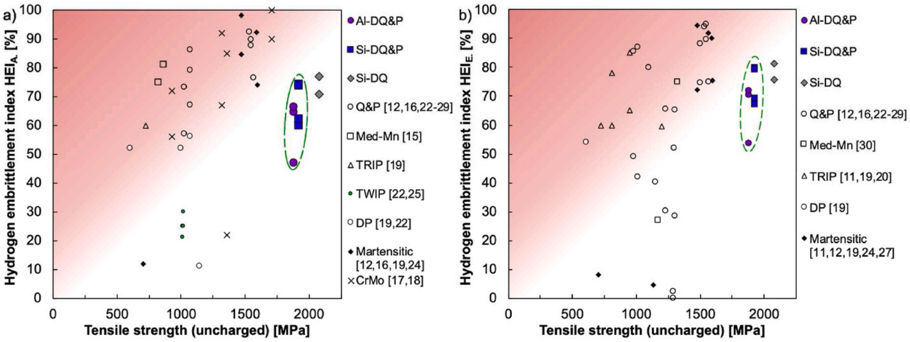

Fig. 8. Comparison of HE susceptibility of high-strength steels with nominal uncharged tensile strength and a) hydrogen embrittlement index from area reduction HEI$_{A.}$, and b) hydrogen embrittlement index from loss of elongation HEI$_{E.}$ Green dashed circles highlight the results with DQ&P steels. External data: Q&P [12,16,22–29], *Med-Mn:* [15,30], *other TRIP steels* [11,19,20], *TWIP* [22,25], *DP* [19,22], *Martensitic:* [11,12,19,24,27], *and CrMo* [17,18] steels. (For interpretation of the references to colour in this figure legend, the reader is referred to the Web version of this article.)

HEI values are increasing again due to introduction of the coarser blocky RA. Thus, the here investigated materials hit the sweet-spot in RA – HEI balance, too. However, possible exceptions to these can be highly alloyed Med-Mn steels with higher fractions of coarser laminar microstructures instead of blocky morphologies [65].

To gain better understanding on how to produce industrially relevant hydrogen-tolerant (ultra)high-strength steels, further studies should be targeted towards RA decomposition and its influence on H uptake, and alternative to SSRT testing, mechanical test methods relevant to structural integrity.

5. Conclusions

We investigated elemental and microstructural effects on hydrogen embrittlement in 2 GPa direct-quenched and partitioned (DQ&P) martensitic-austenitic steels based on Si and Al alloying and with comparison to an essentially martensitic direct-quenched (DQ) steel to elucidate the effect of retained austenite (RA) film thickness and bcc alloy-enrichment on susceptibility to hydrogen embrittlement. The main conclusions based on our experimental and theoretical findings in the absence of detrimental blocky RA are.

- Increasing RA film thickness improves tolerance to hydrogen embrittlement (HE), but increase in RA vol% alone is relatively ineffective within Si-based alloying. Al-based bcc stabilisation facilitates exceptional mitigation of HE susceptibility with the same processing and similar mechanical properties.
- Benefits of Al-based alloying are two-fold: increased RA film-thickness can tolerate higher hydrogen contents, and Al-alloyed bcc drives H to fcc more effectively than Si-bcc.
- DFT study revealed that the solubility of H is dramatically increased in fcc Fe when H and C are present as second neighbours. Thus, higher C content in RA in DQ&P steels increases trapping of H thereby resulting in less diffusible H than in low-RA DQ, which explains the experimental differences in H permeation.
- DFT calculations confirm that H solubility is higher in bcc Fe in the presence of Si rather than Al, suggesting less H in fcc in Si-DQ&P. This is in good agreement with the TDS results. The combined findings explain the experimental observation of Al-DQ&P being more HE resistant than Si-DQ&P.

CRediT authorship contribution statement

Sakari Pallaspuro: Writing – review & editing, Writing – original draft, Visualization, Validation, Resources, Project administration, Methodology, Investigation, Formal analysis, Data curation, Conceptualization. **Eric Fangnon:** Writing – original draft, Investigation. **S. Assa Aravindh:** Writing – original draft, Validation, Software, Methodology, Investigation, Formal analysis, Conceptualization. **Lisa Claeys:** Writing – review & editing, Validation, Investigation, Formal analysis. **Renata Latypova:** Writing – original draft, Validation, Methodology, Investigation, Formal analysis. **Yuriy Yagodzinsky:** Investigation, Data curation. **Niko Aho:** Formal analysis. **Pekka Kantanen:** Resources, Investigation. **Sampo Uusikallio:** Resources, Investigation. **Tom Depover:** Writing – review & editing, Validation, Resources. **Marko Huttula:** Supervision, Funding acquisition. **Poulumi Dey:** Writing – original draft, Validation, Methodology, Conceptualization. **Jukka Kömi:** Project administration, Funding acquisition.

Declaration of competing interest

The authors declare that they have no known competing financial interests or personal relationships that could have appeared to influence the work reported in this paper.

Data availability

Data will be made available on request.

Acknowledgements

This research was supported by Business Finland Oy through the project FOSSA II – Fossil-Free Steel Applications (Dno. 5562/31/2023), and the Research Council of Finland (#358422). CSC - IT center for Science, Finland, is thanked for computational resources. The authors wish to thank S. Saukko of the University of Oulu for operating the TEM, and the technical staff of the Materials and Mechanical Engineering unit at the University of Oulu, namely T.T. Nyo, J. Paavola, and I. Alasaarela, for their help with the experiments and sample preparation.

APPENDIX A

Table A1
Hydrogen-charging parameters and total hydrogen concentrations C_H.

	C_H [wppm]	Suspension	Applied potential [V_{SCE}]	Corrosive potential [mV]	Charging time [h]	Initial current [mA]	Final current [mA]
Al-DQ&P, pre-charge	1.21	3 % NaCl + 0.1 % NH4SCN	−1.0	–	3.0	–	–
Al-DQ&P, in air	0.25	–	–	–	–	NA	NA
Al-DQ&P, H 4.2	4.23	3 % NaCl + 0.3 % NH4SCN	−1.0	−630	2.0	5.0	2.30
Al-DQ&P, H 5.1	5.07	3 % NaCl + 0.3 % NH4SCN	−1.2	−646	2.5	13.0	6.00
Al-DQ&P, H 5.7	5.67	3 % NaCl + 0.3 % NH4SCN	−1.2	−659	2.5	15.0	12.50
Si-DQ&P, pre-charge	0.94	3 % NaCl + 0.1 % NH4SCN	−1.0	–	3.0	–	–
Si-DQ&P, in air	0.21	–	–	NA	–	NA	NA
Si-DQ&P, H 1.6	1.64	3 % NaCl + 0.1 % NH4SCN	−1.0	−455	2.0	3.0	1.80
Si-DQ&P, H 1.7	1.72	3 % NaCl + 0.1 % NH4SCN	−1.0	−463	2.0	4.0	1.80
Si-DQ&P, H 2.0	1.97	3 % NaCl + 0.1 % NH4SCN	−1.2	−483	2.0	9.0	7.00
Si-DQ&P, H 3.0	2.98	3 % NaCl + 0.3 % NH4SCN	−1.0	−665	4.0	2.0	1.90
Si-DQ, pre-charge	0.90	3 % NaCl + 0.1 % NH4SCN	−1.0	–	3.0	–	–
Si-DQ, in air	0.18	–	–	NA	–	NA	NA
Si-DQ, H 1.3	1.34	3 % NaCl + 0.1 % NH4SCN	−1.0	−454	2.0	3.0	1.40
Si-DQ, H 1.4	1.42	3 % NaCl + 0.1 % NH4SCN	−1.0	−513	2.0	5.0	1.80

References

[1] A. Pineau, A. Amine Benzerga, T. Pardoen, Failure of metals III: fracture and fatigue of nanostructured metallic materials, Acta Mater. 107 (2016) 508–544, https://doi.org/10.1016/j.actamat.2015.07.049.

[2] B. Sun, A. Kwiatkowski da Silva, Y. Wu, Y. Ma, H. Chen, C. Scott, D. Ponge, D. Raabe, Physical metallurgy of medium-Mn advanced high-strength steels, Int. Mater. Rev. (2022), https://doi.org/10.1080/09506608.2022.2153220.

[3] J. Kömi, P. Karjalainen, D. Porter, Direct-Quenched Structural Steels, CRC Press, 2016, https://doi.org/10.1081/E-EISA-120049737.

[4] P. Kantanen, M. Somani, A. Kaijalainen, O. Haiko, D. Porter, J. Kömi, Microstructural characterization and mechanical properties of direct quenched and partitioned high-aluminum and high-silicon steels, Metals 9 (2019) 256, https://doi.org/10.3390/met9020256.

[5] S. Wang, A.A. Kistanov, G. King, S. Ghosh, H. Singh, S. Pallaspuro, A. Rahemtulla, M. Somani, J. Kömi, W. Cao, M. Huttula, In-situ quantification and density functional theory elucidation of phase transformation in carbon steel during quenching and partitioning, Acta Mater. 221 (2021), https://doi.org/10.1016/J.ACTAMAT.2021.117361.

[6] S. Ghosh, P. Kaikkonen, V. Javaheri, A. Kaijalainen, I. Miettunen, M. Somani, J. Kömi, S. Pallaspuro, Design of tough, ductile direct quenched and partitioned advanced high-strength steel with tailored silicon content, J. Mater. Res. Technol. 17 (2022) 1390–1407, https://doi.org/10.1016/J.JMRT.2022.01.073.

[7] S. Pallaspuro, A.-C. Hesse, T. Engelke, J. Sainio, S. Ghosh, V. Javaheri, K. Dilger, J. Kömi, Impact toughness of an electron-beam welded 0.2C direct-quenched and partitioned steel, Procedia Struct. Integr. 42 (2022) 895–902, https://doi.org/10.1016/j.prostr.2022.12.113.

[8] E. Akiyama, K. Matsukado, M. Wang, K. Tsuzaki, Evaluation of hydrogen entry into high strength steel under atmospheric corrosion, Corros Sci 52 (2010) 2758–2765, https://doi.org/10.1016/J.CORSCI.2009.11.046.

[9] T. Hageman, E. Martínez-Pañeda, An electro-chemo-mechanical framework for predicting hydrogen uptake in metals due to aqueous electrolytes, Corros Sci 208 (2022) 110681, https://doi.org/10.1016/J.CORSCI.2022.110681.

[10] M. Wang, E. Akiyama, K. Tsuzaki, Effect of hydrogen on the fracture behavior of high strength steel during slow strain rate test, Corros Sci 49 (2007) 4081–4097, https://doi.org/10.1016/J.CORSCI.2007.03.038.

[11] J.A. Ronevich, J.G. Speer, D.K. Matlock, Hydrogen embrittlement of commercially produced advanced high strength sheet steels. SAE Technical Papers, 2010, pp. 255–267, https://doi.org/10.4271/2010-01-0447.

[12] G. Lovicu, E.P. Bagliani, M. Sanctis, A. Dimatteo, R. Ishak, R. Valentini, Hydrogen embrittlement of a medium carbon Q&P steel | Semantic Scholar, La Metall. Ital. 105 (2013) 3–10.

[13] S.L.I. Chan, H.L. Lee, J.R. Yang, Effect of retained austenite on the hydrogen content and effective diffusivity of martensitic structure, Metall. Trans. A 22 A (1991) 2579–2586, https://doi.org/10.1007/BF02851351/METRICS.

[14] L.C.D. Fielding, E.J. Song, D.K. Han, H.K.D.H. Bhadeshia, D.W. Suh, Hydrogen diffusion and the percolation of austenite in nanostructured bainitic steel, Proc. R. Soc. A 470 (2014), https://doi.org/10.1098/RSPA.2014.0108.

[15] Y. Du, X. Gao, L. Lan, X. Qi, H. Wu, L. Du, R.D.K. Misra, Hydrogen embrittlement behavior of high strength low carbon medium manganese steel under different heat treatments, Int. J. Hydrogen Energy 44 (2019) 32292–32306, https://doi.org/10.1016/J.IJHYDENE.2019.10.103.

[16] W. Ding, K. Yang, Y. Gong, L. Wang, J. yao Hong, W. Li, X. jun Jin, Improving hydrogen embrittlement resistance of a modified press hardening steel by introducing retained austenite as hydrogen trap, J. Iron Steel Res. Int. 29 (2022) 1864–1872, https://doi.org/10.1007/S42243-021-00738-4/TABLES/3.

[17] M. Gojie, L. Kosec, The susceptibility to the hydrogen embrittlement of low alloy Cr and CrMo steels, ISIJ Int. 37 (1997) 412–418, https://doi.org/10.2355/ISIJINTERNATIONAL.37.412.

[18] X. Jin, L. Xu, W. Yu, K. Yao, J. Shi, M. Wang, The effect of undissolved and temper-induced (Ti,Mo)C precipitates on hydrogen embrittlement of quenched and tempered Cr-Mo steel, Corros Sci 166 (2020) 108421, https://doi.org/10.1016/J.CORSCI.2019.108421.

[19] T. Depover, D. Pérez Escobar, E. Wallaert, Z. Zermout, K. Verbeken, Effect of hydrogen charging on the mechanical properties of advanced high strength steels, Int. J. Hydrogen Energy 39 (2014) 4647–4656, https://doi.org/10.1016/J.IJHYDENE.2013.12.190.

[20] T. Hojo, R. Kikuchi, H. Waki, F. Nishimura, Y. Ukai, E. Akiyama, Effect of strain rate on the hydrogen embrittlement property of ultra high-strength low alloy TRIP-aided steel, ISIJ Int. 58 (2018) 751–759, https://doi.org/10.2355/isijinternational.ISIJINT-2017-576.

[21] K.G. Solheim, J.K. Solberg, J. Walmsley, F. Rosenqvist, T.H. Bjørnå, The role of retained austenite in hydrogen embrittlement of supermartensitic stainless steel, Eng. Fail. Anal. 34 (2013) 140–149, https://doi.org/10.1016/J.ENGFAILANAL.2013.07.025.

[22] Q. Liu, Q. Zhou, J. Venezuela, M. Zhang, A. Atrens, Evaluation of the influence of hydrogen on some commercial DP, Q&P and TWIP advanced high-strength steels during automobile service, Eng. Fail. Anal. 94 (2018) 249–273, https://doi.org/10.1016/J.ENGFAILANAL.2018.08.011.

[23] X. Zhu, W. Li, H. Zhao, L. Wang, X. Jin, Hydrogen trapping sites and hydrogen-induced cracking in high strength quenching & partitioning (Q&P) treated steel, Int. J. Hydrogen Energy 39 (2014) 13031–13040, https://doi.org/10.1016/j.ijhydene.2014.06.079.

[24] J. Yang, F. Huang, Z. Guo, Y. Rong, N. Chen, Effect of retained austenite on the hydrogen embrittlement of a medium carbon quenching and partitioning steel with

refined microstructure, Mater. Sci. Eng., A 665 (2016) 76–85, https://doi.org/10.1016/J.MSEA.2016.04.025.

[25] Q. Liu, Q. Zhou, J. Venezuela, M. Zhang, A. Atrens, Hydrogen influence on some advanced high-strength steels, Corros Sci 125 (2017) 114–138, https://doi.org/10.1016/J.CORSCI.2017.06.012.

[26] Z. Wang, M. Huang, Improving hydrogen embrittlement resistance of hot-stamped 1500 MPa steel parts that have undergone a Q&P treatment by the design of retained austenite and martensite matrix, Metals 10 (2020) 1585, https://doi.org/10.3390/MET10121585, 10 (2020) 1585.

[27] W.Y. Zhao, W.J. Chen, Z.Z. Zhao, S. Kuang, J.B. Liu, L. Sun, Study on the hydrogen-induced delayed fracture behavior of Q-P980 and MS980, Mater. Res. Express 8 (2021) 126510, https://doi.org/10.1088/2053-1591/AC3BF6.

[28] F. Vercruysse, L. Claeys, T. Depover, P. Verleysen, R.H. Petrov, K. Verbeken, The effect of Nb on the hydrogen embrittlement susceptibility of Q&P steel under static and dynamic loading, Mater. Sci. Eng., A 852 (2022) 143652, https://doi.org/10.1016/J.MSEA.2022.143652.

[29] P. Xu, C. Li, W. Li, M. Zhu, K. Zhang, Effect of microstructure on hydrogen embrittlement susceptibility in quenching-partitioning-tempering steel, Mater. Sci. Eng., A 831 (2022) 142046, https://doi.org/10.1016/J.MSEA.2021.142046.

[30] B. Sun, W. Krieger, M. Rohwerder, D. Ponge, D. Raabe, Dependence of hydrogen embrittlement mechanisms on microstructure-driven hydrogen distribution in medium Mn steels, Acta Mater. 183 (2020) 313–328, https://doi.org/10.1016/J.ACTAMAT.2019.11.029.

[31] J. Chiang, B. Lawrence, J.D. Boyd, A.K. Pilkey, Effect of microstructure on retained austenite stability and work hardening of TRIP steels, Mater. Sci. Eng., A 528 (2011) 4516–4521, https://doi.org/10.1016/J.MSEA.2011.02.032.

[32] B. He, On the factors governing austenite stability: intrinsic versus extrinsic, Materials 13 (2020) 3440, https://doi.org/10.3390/MA13153440, 13 (2020) 3440.

[33] G. Kumar, S. Ghosh, S. Pallaspuro, M.C. Somani, J. Kömi, S.K. Mishra, A. A. Gokhale, Fracture toughness characteristics of thermo-mechanically rolled direct quenched and partitioned steels, Mater. Sci. Eng., A 840 (2022) 142788, https://doi.org/10.1016/J.MSEA.2022.142788.

[34] S. Vander Vennet, S. Leitner, V. Razumovskiy, W. Ecker, T. Depover, K. Verbeken, Mechanical load induced hydrogen charging of retained austenite in quenching and partitioning (Q&P) steel, Int. J. Hydrogen Energy 48 (2023) 2428–2441, https://doi.org/10.1016/J.IJHYDENE.2022.10.119.

[35] M.C. Somani, D.A. Porter, L. Pentti Karjalainen, D.K. Misra, Evaluation of DQ&P processing route for the development of ultra-high strength tough ductile steels, Int. J. Metall. Eng. 2 (2013) 154–160, https://doi.org/10.5923/j.ijmee.20130202.07.

[36] O. Barrera, D. Bombac, Y. Chen, T.D. Daff, E. Galindo-Nava, P. Gong, D. Haley, R. Horton, I. Katzarov, J.R. Kermode, C. Liverani, M. Stopher, F. Sweeney, Understanding and mitigating hydrogen embrittlement of steels: a review of experimental, modelling and design progress from atomistic to continuum, J. Mater. Sci. 53 (2018) 6251–6290, https://doi.org/10.1007/S10853-017-1978-5.

[37] E.J. Song, H.K.D.H. Bhadeshia, D.W. Suh, Interaction of aluminium with hydrogen in twinning-induced plasticity steel, Scripta Mater. 87 (2014) 9–12, https://doi.org/10.1016/J.SCRIPTAMAT.2014.06.007.

[38] L. Ismer, T. Hickel, J. Neugebauer, Ab initio study of the solubility and kinetics of hydrogen in austenitic high Mn steels, Phys. Rev. B Condens. Matter 81 (2010) 094111, https://doi.org/10.1103/PHYSREVB.81.094111/FIGURES/8/MEDIUM.

[39] Y.A. Du, L. Ismer, J. Rogal, T. Hickel, J. Neugebauer, R. Drautz, First-principles study on the interaction of H interstitials with grain boundaries in α- and γ-Fe, Phys. Rev. B Condens. Matter 84 (2011) 144121, https://doi.org/10.1103/PHYSREVB.84.144121/FIGURES/13/MEDIUM.

[40] T.A. Timmerscheidt, P. Dey, D. Bogdanovski, J. von Appen, T. Hickel, J. Neugebauer, R. Dronskowski, The role of κ-carbides as hydrogen traps in high-Mn steels, Metals 7 (2017) 264, https://doi.org/10.3390/MET7070264, 7 (2017) 264.

[41] R. Latypova, T.T. Nyo, O. Seppälä, K. Hahtonen, H. Hänninen, J. Kömi, S. Pallaspuro, The effect of Pd and Ni coatings on hydrogen permeation experiments of as-quenched martensitic steel, Corrosion Rev. 0 (2023), https://doi.org/10.1515/CORRREV-2022-0118.

[42] Q. Liu, Q. Zhou, J. Venezuela, M. Zhang, J. Wang, A. Atrens, A review of the influence of hydrogen on the mechanical properties of DP, TRIP, and TWIP advanced high-strength steels for auto construction, Corrosion Rev. 34 (2016) 127–152, https://doi.org/10.1515/CORRREV-2015-0083/ASSET/GRAPHIC/J_CORRREV-2015-0083_CV_006.JPG.

[43] Q. Liu, A. Atrens, Reversible hydrogen trapping in a 3.5NiCrMoV medium strength steel, Corros Sci 96 (2015) 112–120, https://doi.org/10.1016/J.CORSCI.2015.04.011.

[44] H. Tervo, A. Kaijalainen, T. Pikkarainen, S. Mehtonen, D. Porter, Effect of impurity level and inclusions on the ductility and toughness of an ultra-high-strength steel, Mater. Sci. Eng. 697 (2017) 184–193, https://doi.org/10.1016/J.MSEA.2017.05.013.

[45] D.J. Dyson, B. Holmes, Effect of alloying additions on the lattice parameter of austenite, Journal of Iron and Steel Institute 208 (1970) 469–474. https://jglobal.jst.go.jp/en/detail?JGLOBAL_ID=201602012628629248. (Accessed 3 June 2022).

[46] G. Kresse, Ab initio molecular dynamics for liquid metals, J. Non-Cryst. Solids 192–193 (1995) 222–229, https://doi.org/10.1016/0022-3093(95)00355-X.

[47] G. Kresse, J. Furthmüller, Efficiency of ab-initio total energy calculations for metals and semiconductors using a plane-wave basis set, Comput. Mater. Sci. 6 (1996) 15–50, https://doi.org/10.1016/0927-0256(96)00008-0.

[48] G. Kresse, D. Joubert, From ultrasoft pseudopotentials to the projector augmented-wave method, Phys. Rev. B 59 (1999) 1758, https://doi.org/10.1103/PhysRevB.59.1758.

[49] J.P. Perdew, K. Burke, M. Ernzerhof, Generalized gradient approximation made simple, Phys. Rev. Lett. 77 (1996) 3865, https://doi.org/10.1103/PhysRevLett.77.3865.

[50] J.H. Ryu, Y.S. Chun, C.S. Lee, H.K.D.H. Bhadeshia, D.W. Suh, Effect of deformation on hydrogen trapping and effusion in TRIP-assisted steel, Acta Mater. 60 (2012) 4085–4092, https://doi.org/10.1016/J.ACTAMAT.2012.04.010.

[51] A. Turk, G.R. Joshi, M. Gintalas, M. Callisti, P.E.J. Rivera-Díaz-del-Castillo, E. I. Galindo-Nava, Quantification of hydrogen trapping in multiphase steels: Part I – point traps in martensite, Acta Mater. 194 (2020) 118–133, https://doi.org/10.1016/J.ACTAMAT.2020.05.007.

[52] A. Turk, S.D. Pu, D. Bombač, P.E.J. Rivera-Díaz-del-Castillo, E.I. Galindo-Nava, Quantification of hydrogen trapping in multiphase steels: Part II – effect of austenite morphology, Acta Mater. 197 (2020) 253–268, https://doi.org/10.1016/J.ACTAMAT.2020.07.039.

[53] K. Takai, R. Watanuki, Hydrogen in trapping states innocuous to environmental degradation of high-strength steels, ISIJ Int. 43 (2003) 520–526, https://doi.org/10.2355/ISIJINTERNATIONAL.43.520.

[54] H.H. Podqurski, R.A. Oriani, Nitrogenation of Fe-Al alloys, Absorption of hydrogen in nitrogenated Fe-Al alloys, Metall. Trans. A 3 (1972) 2055.

[55] J.L. Lee, J.Y. Lee, INTERACTION OF HYDROGEN WITH THE INTERFACE OF Al2O3 PARTICLES IN IRON, Metall. Trans. A 17 A (1986) 2183–2186, https://doi.org/10.1007/BF02645916/METRICS.

[56] R. Latypova, O. Seppälä, T. Tun Nyo, T. Kauppi, S. Mehtonen, H. Hänninen, J. Kömi, S. Pallaspuro, Influence of prior austenite grain structure on hydrogen-induced fracture in as-quenched martensitic steels, Eng. Fract. Mech. 281 (2023) 109090, https://doi.org/10.1016/J.ENGFRACMECH.2023.109090.

[57] T. Hickel, R. Nazarov, E.J. McEniry, G. Leyson, B. Grabowski, J. Neugebauer, Ab initio based understanding of the segregation and diffusion mechanisms of hydrogen in steels, J. Occup. Med. 66 (2014) 1399–1405, https://doi.org/10.1007/S11837-014-1055-3/FIGURES/3.

[58] A.S. Kholtobina, R. Pippan, L. Romaner, D. Scheiber, W. Ecker, V.I. Razumovskiy, Hydrogen trapping in bcc iron, Materials 13 (2020) 2288, https://doi.org/10.3390/MA13102288, 13 (2020) 2288.

[59] S.A. Danilkin, H. Fuess, H. Wipf, A. Ivanov, V.G. Gavriljuk, D. Delafosse, T. Magnin, Hydrogen vibrations in austenitic fcc Fe-Cr-Mn-Ni steels, Europhys. Lett. 63 (2003) 69, https://doi.org/10.1209/EPL/I2003-00479-1.

[60] X.C. Xiong, B. Chen, M.X. Huang, J.F. Wang, L. Wang, The effect of morphology on the stability of retained austenite in a quenched and partitioned steel, Scripta Mater. 68 (2013) 321–324, https://doi.org/10.1016/J.SCRIPTAMAT.2012.11.003.

[61] H.K.D.H. Bhadeshia, Prevention of hydrogen embrittlement in steels, ISIJ Int. 56 (2016) 24–36, https://doi.org/10.2355/ISIJINTERNATIONAL.ISIJINT-2015-430.

[62] A. Troiano, Hydrogen Embrittlement and Stress Corrosion Cracking, ASM International, 1985.

[63] S. Wang, M.L. Martin, P. Sofronis, S. Ohnuki, N. Hashimoto, I.M. Robertson, Hydrogen-induced intergranular failure of iron, Acta Mater. 69 (2014) 275–282, https://doi.org/10.1016/J.ACTAMAT.2014.01.060.

[64] Y. Ding, H. Yu, K. Zhao, M. Lin, S. Xiao, M. Ortiz, J. He, Z. Zhang, Hydrogen-induced transgranular to intergranular fracture transition in bi-crystalline nickel, Scripta Mater. 204 (2021) 114122, https://doi.org/10.1016/J.SCRIPTAMAT.2021.114122.

[65] M. Wang, C.C. Tasan, M. Koyama, D. Ponge, D. Raabe, Enhancing hydrogen embrittlement resistance of lath martensite by introducing nano-films of interlath austenite, Metall Mater Trans A Phys Metall Mater Sci 46 (2015) 3797–3802, https://doi.org/10.1007/S11661-015-3009-Y/FIGURES/4.